



Joint capacity of bonded sleeve connections for tubular fibre reinforced polymer members



Chengyu Qiu^a, Peng Feng^b, Yue Yang^b, Lei Zhu^c, Yu Bai^{a,*}

^a Department of Civil Engineering, Monash University, Clayton, VIC 3800, Australia

^b Department of Civil Engineering, Tsinghua University, Beijing 100084, China

^c School of Civil and Transportation Engineering, Beijing Higher Institution Engineering Research Center of Structural Engineering and New Materials, Beijing University of Civil Engineering and Architecture, Beijing 100044, China

ARTICLE INFO

Article history:

Received 5 September 2016

Revised 8 November 2016

Accepted 5 December 2016

Available online 18 December 2016

Keywords:

Fibre reinforced polymer

Sleeve connection

Adhesive bonding

Shear stress distribution

Joint capacity

ABSTRACT

Bonded sleeve joints formed by telescoping a steel tube connector for bolt-fastening are effective means for assembling tubular fibre reinforced polymer (FRP) members into more complex structures such as planar or space frames. A theoretical formulation is developed in this paper to estimate the capacity of such joints in axial loading and the predictions are validated by experimental results covering various section geometries and bond lengths. The formulation is based on the bilinear bond-slip constitutive relationship considering elastic, softening and debonding behaviour at the adhesive bonding region. Finite element (FE) analysis is also conducted to estimate the joint capacity and to describe shear stress distribution in the adhesive layer, validating the reliability of the theoretic results. The theoretical formulation is therefore further used to study the effects of design parameters including bond length and adherend stiffness ratio, again validated by FE results. An effective bond length can be accurately predicted by the theoretical formulation for the joint capacity at both the elastic limit and the ultimate state. Given a bond length, an optimal adherend stiffness ratio can be identified to achieve the maximum joint capacity at the elastic limit or the ultimate state.

© 2016 Elsevier Ltd. All rights reserved.

1. Introduction

With virtues such as high strength-to-weight ratio, superior corrosion resistance and low maintenance requirements, fibre reinforced polymer (FRP) structural members have gained broad recognition in the construction industry [1,2]. In particular, glass FRP (GFRP) composites, with sufficient strength and stiffness at moderate cost, have received acceptance as construction materials for structural members [3–5]. Aided by the pultrusion manufacturing technique [6,7], mass production of GFRP structural components with constant cross-section has been facilitated at reduced cost and with satisfactory quality control. Such components have been employed as bridge decks [8–11], reinforcements [12], roof structures [13], trusses [14], floor systems [15–17], and components in hybrid members [18–20], in shapes of open or closed section. However, their application in structural construction still requires the development of reliable and convenient connection approaches, especially for tubular sections.

Early efforts to develop connections for GFRP tubular sections imitated practices in steel structures, for example, using bolted-through web-gusset plates or flange-angle cleats for beam-column connections [21]. Later, a cuff connection for pultruded GFRP tubular sections was proposed and demonstrated enhanced strength and stiffness [22,23]. Recently, the benefits of a sleeve connection formed by telescoping steel and GFRP tubular members have been underlined for applications in space frame structures [24]. The steel sleeve connector not only enables versatile connection forms but also provides ductile failure mode through steel yielding. In such connections, the GFRP-steel telescoping portion or the sleeve portion acts compositely through adhesive bonding [25] or mechanical fastening [26,27]. Although mechanical fastening facilitates convenient in-situ fabrication, its employment in fixing sleeve joints exposes the relatively weak shear strength of anisotropic GFRP materials and such use becomes inapplicable when circular profiles are used. If adhesive bonding is used, a more uniform stress transfer to GFRP materials is achieved. Bonded sleeve connections have also been developed into beam-to-column scenario [28], where pultruded GFRP and steel tubular square members were used. Such bonded sleeve connections have exhibited significant improvement in both stiffness and strength in

* Corresponding author.

E-mail address: yu.bai@monash.edu (Y. Bai).

comparison with traditional steel angle connections and bolted sleeve connections.

Bonded sleeve connections transfer axial loading through shear between the GFRP and steel adherends. As a special type of bonded lap joint, the joint capacity may be determined through the shear mechanism of the adhesive bonding when the adherends (steel and GFRP in this case) are sufficiently strong. Pioneering theoretical works on single and double lap adhesive-bonded joints have been conducted to understand such shear mechanisms where only elastic [29,30] or elastic-plastic [31,32] bonding behaviour was considered. Joint capacity was therefore evaluated against allowable material stress or strain at critical regions. These approaches are limited to identifying possible failure location or initiation.

Fracture mechanics-based approaches were further introduced to understand the full range behaviour of several types of single and double lap joints. This required understanding of the nonlinear bond-slip relationship at the bonded region. Simplification of the nonlinear bond-slip relationship into a bilinear form enabled the development of closed form analytical solutions for joint capacity and shear stress distribution in the adhesive layer. Such a bilinear relationship is characterised by a linearly ascending stage of shear stress with slip, followed by a linear decrease to zero shear stress at the debonding slip (and slip may further increase while shear stress remains zero). This bilinear relationship was adopted by Ranisch [33] to study the post-cracking behaviour of bonded steel-to-concrete single lap joints subjected to axial loading. By incorporating Volkersen's classical stress analysis and the bilinear bond-slip model, analytical solutions for the capacities of a pull-push plate-to-block bonded joint at elastic and ultimate limit states were developed by Brosens and Van Gemert [34]. This work was further expanded in [35], where analytical solutions were developed to identify several stages of the debonding process. Also utilising the bilinear model, Wu et al. [36] analytically derived the expressions for the joint capacity, adhesive shear stress distribution and the debonding processes of pull-pull and pull-push single lap joints. Experimental investigations were also conducted to understand the debonding behaviour of single and double lap joints, such as steel plate-to-concrete block double lap joint in [37], FRP plate-to-steel pull-push joints in [38], single and double lap FRP plate joints for structural rehabilitation in [39], and single and double lap aluminium plate joints in [40]. Such experimental results were able to validate analytical and numerical models that employed the aforementioned bilinear bond-slip relationship. Furthermore, experimental results of shear stress and slip in the adhesive layer measured from FRP-to-concrete [41,42] and FRP-to-steel bonded lap joints [38,43,44] provided evidence that, when a brittle adhesive was used, the bilinear bond-slip relationship provided a satisfactory approximation to the experimental measurement.

In addition to the bilinear form, several representations of the bond-slip relationships were also proposed to study the behaviour of single and double lap bonded joints. A nonlinear bond-slip curve including softening behaviour was employed by Täljsten [45] for numerical calculation of the capacity of CFRP plate-to-concrete bonded joints; however, it was too sophisticated for analytical derivation, as pointed out by the author. A bond-slip relationship characterised by abrupt failure after the linearly elastic region was adopted by Yuan et al. [35,46]; and a bond-slip relationship with exponential softening behaviour was also considered in the former. For ductile adhesives, bond-slip relationships with trapezoidal shape were considered as more appropriate [44,47]. The load-displacement behaviour of a double lap joint connecting aluminium plates under pull-out test was numerically studied in [48], with consideration of four shapes of bond-slip relationship: bilinear, linear-parabolic, exponential and trapezoidal. It was concluded that, given identical initial stiffness, peak shear stress and fracture energy (as the area under the bond-slip curve) of the bonded inter-

face, the load-displacement behaviour was practically independent of the shape of the bond-slip relationship. It appears that previous analytical and numerical studies have focused mainly on the adhesive shear stress distribution and capacity of adhesive-bonded joints in single or double lap forms. Such responses of a bonded sleeve connection require theoretic understanding and experimental validation to enhance confidence in their application.

This paper therefore formulates theoretical modelling for the joint capacity of a bonded sleeve connection for tubular GFRP members. This theoretic formulation employs the aforementioned well-accepted bilinear bond-slip relationship. Experimental results of joint capacities were obtained from tension tests conducted on steel/GFRP bonded sleeve connection specimens with various cross-section geometries and bond lengths. Finite element (FE) models were also developed for comparison of the joint capacities and shear stress distribution along the bond length. After validation by experimental and FE results, the theoretical formulation was further utilised to investigate the effects of major design parameters including bond length and adherend stiffness ratio, i.e. $E_s A_s / E_g A_g$ where E_s or E_g are the Young's modulus of steel or GFRP, and A_s or A_g are cross-section area of the steel or GFRP component.

2. Summary of experimental results

A series of bonded sleeve joint specimens consisting of a steel tube connector and a GFRP component were prepared and examined, as shown in Fig. 1a–c [24,25]. Their joint capacities were tested for assembly into planar trusses [49] or space frames with assistance of the Octatube nodal joints [25] (Fig. 1d). The tested specimens were categorized into five groups (G1 to G5) based on different cross-sections and geometrical characteristics of steel and GFRP components. Such information is illustrated in Fig. 2 with relevant dimensions provided in Table 1. The material properties of the steel and GFRP components in each group had been measured previously [24,25] and are summarised in Table 1. The adhesive used was Araldite® 420, a two-component epoxy based structural adhesive. Its tensile strength and Young's modulus were tested to be 28.6 MPa and 1.9 GPa; Poisson ratio of 0.36 was obtained [24].

The bonded sleeve connection specimens in G1 and G2 were formed by GFRP rods inserted into steel tubes; those in G3 to G5 were formed by steel tubes inserted into GFRP tubes (Figs. 1 and 2). These groups of specimens cover possible scenarios in practice where the GFRP component may be either the outer [25] or inner adherend [49]. The adoption of GFRP rods instead of tubes in G1 and G2 was to increase their cross section areas thus axial capacities, preventing potential failure of the GFRP component. In G1 to G4, the free ends of the steel tubes were flattened for clamping or bolt-fastening to nodal joints in structural assembly. With a similar purpose, those in G5 were slot-welded with a steel gusset

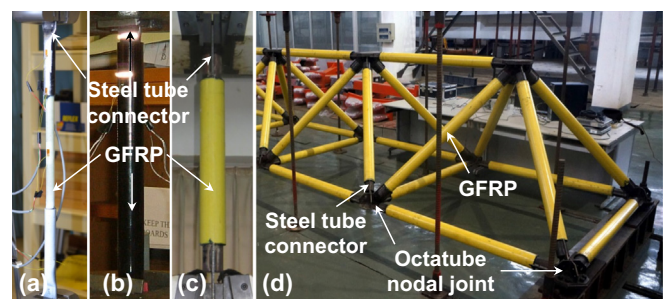


Fig. 1. Bonded sleeve connections for: (a) specimens G1&G2; (b) specimens G3&G4; (c) specimen G5; and (d) an assembled large-scale space frame.

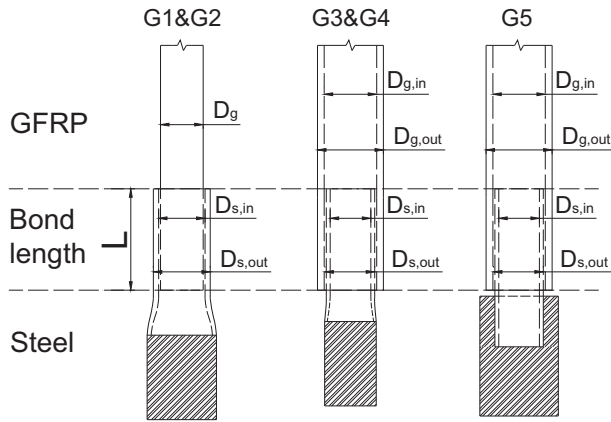


Fig. 2. Geometries of specimens in different groups (magnitudes of the symbols are given in Table 1 for each group).

plate. The specimens were loaded in tension to failure under displacement control. Among all specimens, two types of failure mode were observed, namely pull-out failure (Fig. 3a) and excessive yielding or fracture of the steel tube connector (Fig. 3b). The former failure mode was characterised by adhesive failure close to the inner adherend or interface failure between the adhesive and the inner adherend. Also listed in Table 1 are the bond lengths that incurred pull-out failure within each group of specimens. In Table 2, these specimens are named following the convention of group index and bond length, together with the experimental results of their ultimate joint capacity $P_{u,E}$.

3. Theoretical formulation of joint capacity

3.1. Governing differential equations

Differential governing equations are formulated in this section for adhesive shear stress and adherend normal stress based on Volkersen's stress analysis. When a joint is under axial loading (P), the adhesive layer is predominantly subjected to shear deformation, as illustrated in Fig. 4. Here the outer adherend is presumed to be a GFRP tube and the inner adherend a steel tube (Fig. 4a), though the deduced equilibrium is equally applicable to other materials or to the case in which the inner adherend is a circular rod. Moreover, despite the derivation being based on axial tension, a compression scenario would produce identical force equilibrium. In this study, L , A and b are the bond length, cross-section area and circular circumference of the bonded face respectively; σ , u and ε are axial stress, displacement and strain of adherend; E is Young's modulus and τ is shear stress in the adhesive layer; subscripts 'g' and 's' denote the material of GFRP or steel.

A few assumptions or simplifications are made in the derivation. Adherends are linear elastic thus the formulation is valid before yielding of the steel tube. Normal stress is assumed uni-

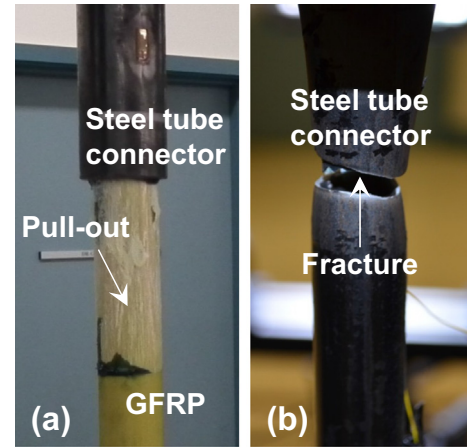


Fig. 3. Typical failure modes of bonded sleeve connection specimens: (a) pull-out failure; (b) fracture of steel tube connector.

formly distributed over the cross-section of adherends. The adhesive layer is thin compared to the thickness of the adherend; therefore shear stress is considered uniform through the thickness of adhesive. Cross-sections of adherends and adhesive are constant along the bonded region.

As a result, the slip between adherends δ is defined as the relative displacement between the GFRP and steel components (Fig. 4b):

$$\delta = u_s - u_g \quad (1)$$

where u_s and u_g are the axial displacement of the steel and GFRP adherend respectively.

Taking derivatives of δ with respect to x gives:

$$\frac{d\delta}{dx} = \frac{du_s}{dx} - \frac{du_g}{dx} = \frac{\sigma_s}{E_s} - \frac{\sigma_g}{E_g} \quad (2)$$

$$\frac{d^2\delta}{dx^2} = \frac{d^2u_s}{dx^2} - \frac{d^2u_g}{dx^2} \quad (3)$$

For a differential length of the steel tube (Fig. 4b), the shear stress in the adhesive layer τ and the normal stress in the steel σ_s can be expressed according to force equilibrium in the x direction:

$$\tau b_s dx = A_s d\sigma_s \rightarrow \frac{d\sigma_s}{dx} = \frac{\tau b_s}{A_s} \quad (4)$$

$$\sigma_s = E_s \frac{du_s}{dx} \rightarrow \frac{d\sigma_s}{dx} = E_s \frac{d^2u_s}{dx^2} \quad (5)$$

Likewise, for a differential length of GFRP tube (Fig. 4b) shear stress in the adhesive layer τ and normal stress in the GFRP σ_g can be expressed accordingly:

Table 1
Geometry and material properties of specimens.

Group	Description	GFRP diameter $D_{g,out}/D_{g,in}$ (mm)	Steel diameter $D_{s,out}/D_{s,in}$ (mm)	Bond length for pull-out failure L (mm)	Young's modulus E (GPa)	Strength (MPa)
G1	GFRP rod into steel	15.5/-	21.3/17.3	30, 40, 50	51.5/198.3	207.0/487.5
G2	tube	25.3/-	33.7/27.5	30, 40, 50, 60, 70, 80	47.4/209.7	207.0/397.4
G3	Steel tube into GFRP	38.0/30.0	26.9/22.3	30, 40	21.6/182.4	240.0/294.7
G4	tube	31.0/24.6	21.3/17.3	30, 40	31.4/198.3	240.0/487.5
G5		92.0/76.0	73.0/65.0	80	39.3/196.8	300.0/451.3

* For GFRP or steel component: outer diameter/inner diameter; for Young's modulus: longitudinal direction of GFRP/steel; for strength: longitudinal tensile strength of GFRP/yield strength of steel.

Table 2
Ultimate joint capacity (P_u) of specimens with the pull-out failure mode.

Specimen	Experiment $P_{u,E}$ (kN)	Theoretical $P_{u,TH}$ (kN)	$P_{u,E}/P_{u,TH}$	Finite element $P_{u,FE}$ (kN)	$P_{u,E}/P_{u,FE}$
G1-30	40.0	33.8	1.183	34.1	1.172
G1-40	48.0	44.2	1.085	43.3	1.109
G1-50	53.0	53.9	0.983	51.6	1.028
<i>G1-60, 70 and 80 failed by fracture of steel</i>					
G2-30	52.0	54.9	0.947	52.5	0.990
G2-40	72.0	72.3	0.996	69.6	1.035
G2-50	82.0	89.0	0.922	85.7	0.957
G2-60	97.0	104.6	0.927	102.7	0.944
G2-70	111.0	119.1	0.932	114.7	0.968
G2-80	116.0	132.1	0.878	125.5	0.924
<i>G2-90 and 100 failed by excessive yielding of steel</i>					
G3-30	41.0	57.4	0.714	52.9	0.776
G3-40	57.0	73.7	0.773	64.9	0.878
<i>G3-50, 60 and 70 failed by fracture of steel</i>					
G4-30	42.0	46.8	0.897	42.5	0.988
G4-40	56.0	60.7	0.922	55.4	1.012
<i>G4-50, 60 and 70 failed by fracture of steel</i>					
G5-80	362.0	387.6	0.934	378.0	0.958
<i>G5-100 failed by fracture of steel</i>					
Mean			0.935		0.981
Standard deviation			0.114		0.095

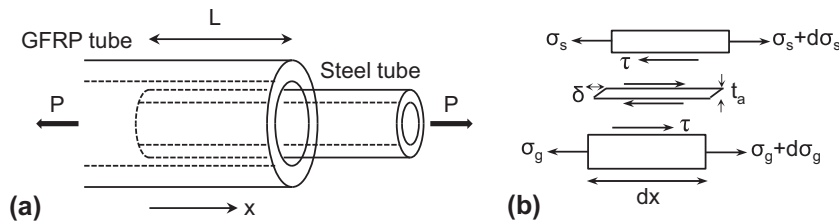


Fig. 4. A circular bonded sleeve connection under axial tension: (a) overall geometry; (b) typical differential element.

$$\tau b_g dx = -A_g d\sigma_g \rightarrow \frac{d\sigma_g}{dx} = -\frac{\tau b_g}{A_g} \quad (6)$$

$$\sigma_g = E_g \frac{du_g}{dx} \rightarrow \frac{d\sigma_g}{dx} = E_g \frac{d^2 u_g}{dx^2} \quad (7)$$

For a full cross-section within the bond length, the force equilibrium in the axial direction gives:

$$\sigma_s A_s + \sigma_g A_g = P \rightarrow \sigma_s = \frac{P - \sigma_g A_g}{A_s} \quad (8)$$

Combining Eqs. (3)–(7), the governing equation for the shear stress in the adhesive layer τ can be formed as:

$$\frac{d^2 \delta}{dx^2} - \left(\frac{b_s}{E_s A_s} + \frac{b_g}{E_g A_g} \right) \tau = 0 \quad (9)$$

Because of the thin adhesive layer, in Eq. (9) the bonded circumference around the steel b_s is approximately equal to that of the GFRP b_g , and both these values can be considered as the centre line perimeter of the adhesive layer. The governing equation for the normal stress in the GFRP component σ_g can be obtained by substituting Eq. (8) into Eq. (2):

$$\sigma_g = \frac{1}{\left(\frac{A_g}{A_s} \frac{1}{E_s} + \frac{1}{E_g} \right)} \left(\frac{P}{E_s A_s} - \frac{d\delta}{dx} \right) \quad (10)$$

Knowing the normal stress in the GFRP component σ_g from Eq. (10), the normal stress in the steel component σ_s can be easily obtained from Eq. (8).

Eqs. (9) and (10) are the governing differential equations for the adhesive shear stress and adherend normal stress of a bonded sleeve joint under axial loading. They are valid regardless of the exact shape of the bond-slip relationship. In the following sections, a bilinear bond-slip relationship is implemented into the governing equations. The stress distributions and corresponding joint capacities are solved under possible cases of boundary conditions.

3.2. Bond-slip relationship of adhesive layer

Fig. 5 shows the bilinear bond-slip relationship for the adhesive-bonded region. Defined by the origin (0, 0), the peak shear stress point (δ_1, τ_f) and the debonding point ($\delta_f, 0$), such a bilinear curve is commonly described with three stages: elastic,

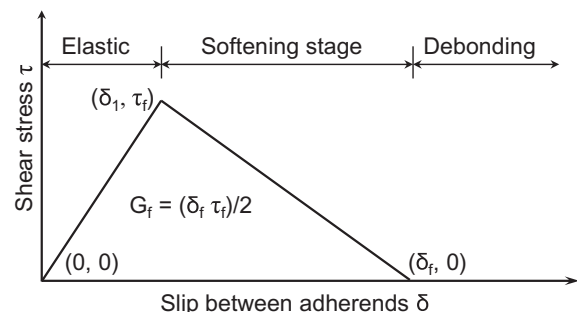


Fig. 5. Typical bilinear bond-slip relationship for adhesive bonding between steel and GFRP.

softening and debonding stages, as indicated in Fig. 5. The area bounded by the curve (i.e. elastic and softening stage) is termed the interface fracture energy (G_f). Eqs. (11) and (12) were used to determine the peak shear stress τ_f and the debonding slip δ_f , according to the correlations formed in [38]. This is because similar adherend materials (steel and pultruded FRP), adhesive thickness (1 to 2 mm) adhesive tensile strength (20 to 30 MPa) and surface preparation of adherends (sandblasted and cleaned with Acetone) were adopted. With the assumption of uniform shear stress through the thickness of adhesive layer, the slip at peak shear stress δ_1 can be obtained from Eq. (13) based on the corresponding shear strain (τ_f/G_a).

$$\tau_f = 0.8f_{t,a} \quad (11)$$

$$\frac{1}{2}\tau_f\delta_f = 31\left(\frac{f_{t,a}}{G_a}\right)^{0.56} t_a^{0.27} \quad (12)$$

$$\delta_1 = \tau_f t_a / G_a \quad (13)$$

where $f_{t,a}$ is the tensile strength of the adhesive; G_a is the shear modulus of the adhesive; and t_a is the thickness of the adhesive layer. In Eq. (12), τ_f , $f_{t,a}$ and G_a are in MPa, δ_f and t_a in mm. As a result, the bond-slip relationship is represented in mathematical form as Eq. (14)

$$\tau = f(\delta) = \begin{cases} \frac{\tau_f}{\delta_1}\delta, & 0 \leq \delta \leq \delta_1 \\ \frac{\tau_f}{\delta_f - \delta_1}(\delta_f - \delta), & \delta_1 \leq \delta \leq \delta_f \\ 0, & \delta_1 \leq \delta \end{cases} \quad (14)$$

where τ and δ are the shear stress in the adhesive layer and slip between the adherends.

As the axial load (P) increases, the joint capacity at the elastic limit (P_e) is attained when any location within the bonded area is loaded to completion of the elastic stage, i.e. when τ reaches τ_f . Further, the joint capacity at the ultimate state is attained when the debonding slip δ_f is reached at either end of the bonded area [35] (i.e. $\delta(x=0 \text{ or } L) = \delta_f$) with softening of only one end ($P_{u,s1}$) or both ends ($P_{u,s2}$), or when the full bond length is loaded to the softening stage ($P_{u,sf}$, i.e. for $0 \leq x \leq L$ and $\delta_1 \leq \delta < \delta_f$). In what follows, the joint capacities are solved for the elastic limit (P_e) and three different scenarios of the ultimate state ($P_{u,s1}$, $P_{u,s2}$ or $P_{u,sf}$). Finally, the joint capacities can be compared to the capacities of the adherends (steel tube connector or GFRP component) before the critical capacity can be determined accordingly.

3.3. Joint capacity P_e at elastic limit

When the applied load P is smaller than P_e , i.e. the slip δ along the bond length is no greater than δ_1 , the entire bond length L remains in the elastic region, i.e. $L = L_e$, where L_e denotes the length of the bonded region at the elastic stage. Fig. 6 presents a typical shear stress distribution along the bond length when $\delta(x=0)$ reaches δ_1 , i.e. the applied load P reaches P_e .

Since $0 \leq \delta < \delta_1$, the corresponding shear stress expression in Eq. (14) can be substituted into Eq. (9) as:

$$\frac{d^2\delta}{dx^2} - \left(\frac{b_s}{E_s A_s} + \frac{b_g}{E_g A_g}\right) \frac{\tau_f}{\delta_1} \delta = 0 \quad (15)$$

The general solution form of Eq. (15) for slip at the elastic stage δ_{el} can be given as

$$\delta_{el}(x) = A_1 \cosh(\lambda_1 x) + B_1 \sinh(\lambda_1 x) \quad (16)$$

where the subscript 'el' refers to the region of bond length at the elastic stage

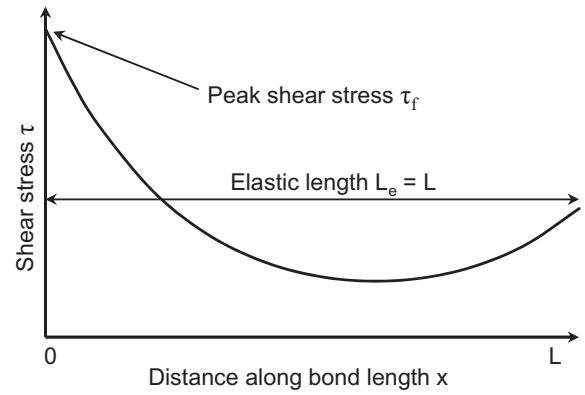


Fig. 6. Typical shear stress distribution when $P = P_e$.

Substituting Eq. (16) into Eq. (10), the normal stress $\sigma_{g,el}$ in the GFRP at the elastic stage of adhesive bonding can be obtained as

$$\sigma_{g,el}(x) = \eta \left[\frac{P}{E_s A_s} - \lambda_1 A \sinh(\lambda_1 x) - \lambda_1 B \cosh(\lambda_1 x) \right] \quad (17)$$

where the constants λ_1 and η are

$$\lambda_1^2 = \left(\frac{b_s}{E_s A_s} + \frac{b_g}{E_g A_g} \right) \frac{\tau_f}{\delta_1} \quad (18)$$

$$\eta = \frac{1}{\left(\frac{A_g}{A_s} \frac{1}{E_s} + \frac{1}{E_g} \right)} \quad (19)$$

By substituting the boundary conditions (Eqs. (20) and (21)) at the two free ends of the bond length

$$\sigma_{g,el}(x=0) = \frac{P}{A_g} \quad (20)$$

$$\sigma_{g,el}(x=L) = 0 \quad (21)$$

The unknown constants A_1 and B_1 can be solved as:

$$A_1 = \frac{P}{\lambda_1} \left[\frac{1}{E_s A_s \sinh(\lambda_1 L)} - \frac{1}{\tanh(\lambda_1 L)} \left(\frac{1}{E_s A_s} - \frac{1}{\eta A_g} \right) \right] \quad (22)$$

$$B_1 = \frac{P}{\lambda_1} \left(\frac{1}{E_s A_s} - \frac{1}{\eta A_g} \right) \quad (23)$$

P_e is then obtained when δ_{el} at either end ($x=0$ or L) reaches δ_1 and the shear stress along the bond length $\tau(x)$ when $0 \leq P \leq P_e$ can be obtained as

$$\tau(x) = \frac{\tau_f}{\delta_1} \delta_{el}(x) \quad 0 \leq x \leq L \quad (24)$$

3.4. Joint capacity $P_{u,s1}$ at ultimate state for softening of only one end

A bonded sleeve joint may reach its ultimate capacity $P_{u,s1}$ (the subscript 's1' denotes softening of one end) when the debonding slip δ_f is attained at one end while the other remains in the elastic stage (i.e. δ at this end is no greater than δ_1). The full bond length L in this case can be divided into two portions: the softening length L_s where the τ - δ relationship has entered the softening stage, and the elastic length L_e where the τ - δ relationship remains at the elastic stage (Fig. 7). If the steel component is stiffer than the GFRP component (i.e. $E_s A_s > E_g A_g$), the GFRP end of the bonded area may be subjected to a higher level of slip between adherends [29,32]. Fig. 7 depicts a typical shear stress distribution along the

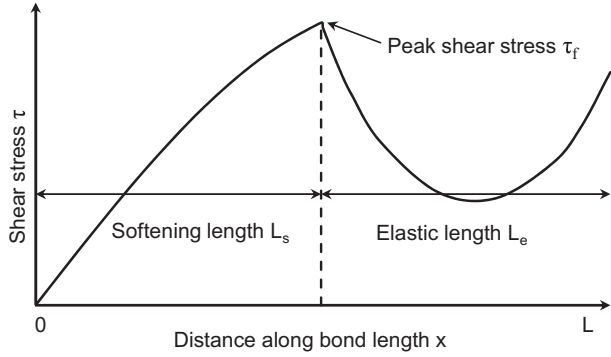


Fig. 7. Typical shear stress distribution when $P = P_{u,s1}$ (softening of only one end).

bond length when δ reaches δ_f at the GFRP end and the corresponding applied load P therefore reaches the ultimate load $P_{u,s1}$.

Within the elastic length, i.e. $L_s < x \leq L$, and based on Eqs. (15) and (16), the slip between adherends δ_{el} and normal stress in the GFRP component $\sigma_{g,el}$ can be expressed as:

$$\delta_{el}(x) = A_2 \cosh[\lambda_1(x - L_s)] + B_2 \sinh[\lambda_1(x - L_s)] \quad (25)$$

$$\sigma_{g,el}(x) = \eta \left(\frac{P_{u,s1}}{E_s A_s} - \lambda_1 A_2 \sinh[\lambda_1(x - L_s)] + \lambda_1 B_2 \cosh[\lambda_1(x - L_s)] \right) \quad (26)$$

Within the softening length, i.e. $0 < x \leq L_s$, the corresponding shear stress expression from Eq. (14) can be substituted into Eq. (9), and Eq. (27) can be obtained as:

$$\frac{d^2 \delta}{dx^2} - \left(\frac{b_s}{E_s A_s} + \frac{b_g}{E_g A_g} \right) \left(\frac{\tau_f}{\delta_f - \delta_1} \right) \delta = \left(\frac{b_s}{E_s A_s} + \frac{b_g}{E_g A_g} \right) \left(\frac{\tau_f}{\delta_f - \delta_1} \right) \delta_f \quad (27)$$

The general solution for δ in Eq. (27) can be formed as:

$$\delta_{sl}(x) = C_1 \sin(\lambda_2 x) + D_1 \sinh(\lambda_2 x) + \delta_f \quad (28)$$

where the subscript 'sl' refers to the region of bond length at the softening stage, and the constant λ_2 is

$$\lambda_2^2 = \left(\frac{b_s}{E_s A_s} + \frac{b_g}{E_g A_g} \right) \left(\frac{\tau_f}{\delta_f - \delta_1} \right) \quad (29)$$

Substituting Eq. (28) into Eq. (10) gives

$$\sigma_{g,sl}(x) = \eta \left[\frac{P_{u,s1}}{E_s A_s} - \lambda_2 C_1 \cos(\lambda_2 x) + \lambda_2 D_1 \sin(\lambda_2 x) \right] \quad (30)$$

where the values of A_2 , B_2 , C_1 , D_1 , $P_{u,s1}$, L_s can be determined by applying the following six boundary conditions:

$$\delta_{sl}(x=0) = \delta_f \quad (31)$$

$$\delta_{el}(x=L_s) = \delta_1 \quad (32)$$

$$\delta_{sl}(x=L_s) = \delta_1 \quad (33)$$

$$\sigma_{g,sl}(x=0) = \frac{P_{u,s1}}{A_g} \quad (34)$$

$$\sigma_{g,el}(x=L) = 0 \quad (35)$$

$$\sigma_{g,el}(x=L_s) = \sigma_{g,sl}(x=L_s) \quad (36)$$

When $P = P_{u,s1}$, the shear stress $\tau(x)$ at a given location x along the bond length can be obtained as:

$$\tau(x) = \begin{cases} \frac{\tau_f}{\delta_f - \delta_1} [\delta_f - \delta_{sl}(x)], & 0 \leq x \leq L_s \\ \frac{\tau_f}{\delta_1} \delta_{el}(x), & L_s < x \leq L \end{cases} \quad (37)$$

When the applied load P is less than $P_{u,s1}$ (while larger than P_e), the values of A_2 , B_2 , C_1 , D_1 and L_s can be obtained by applying Eqs. (32)–(36), and the shear stress $\tau(x)$ and normal stress $\sigma_{g,el}(x)$ can be solved accordingly using Eqs. (25), (26), (28), (30) and (37). It is also necessary to check that the steel end is within the elastic stage (i.e. $\delta_{el}(x=L) < \delta_1$) and the softening length is less than the bond length (i.e. $L_s < L$), for the validity of this ultimate state (when $P = P_{u,s1}$), as softening of the bond length occurs only at one end.

3.5. Joint capacity $P_{u,s2}$ at ultimate state for softening of both ends

This case of the ultimate state represents the scenario when the debonding slip δ_f is attained at one end while the other end is loaded into the softening stage of the bond-slip curve (i.e. $\delta_1 - \leq \delta < \delta_f$). Therefore, the full bond length L can be divided into three portions: with two softening lengths at two ends (L_{s1} at the GFRP end and L_{s2} at the steel end), a portion of the bond length in between remains in the elastic stage (L_e). Fig. 8 shows a typical shear stress distribution for this ultimate state and the divisions of bond length, when the applied load P reaches the ultimate load $P_{u,s2}$ (the subscript 's2' denotes softening of two ends) for this case.

Within the elastic length, i.e. $L_{s1} < x \leq L_{s1} + L_e$ (Fig. 8), and based on Eqs. (25) and (26), the slip δ_{el} between adherends and normal stress $\sigma_{g,el}$ of the GFRP component can be expressed as:

$$\delta_{el}(x) = A_3 \cosh[\lambda_1(x - L_{s1})] + B_3 \sinh[\lambda_1(x - L_{s1})] \quad (38)$$

$$\sigma_{g,el}(x) = \eta \left(\frac{P_{u,s2}}{E_s A_s} - \lambda_1 A_3 \sinh[\lambda_1(x - L_{s1})] + \lambda_1 B_3 \cosh[\lambda_1(x - L_{s1})] \right) \quad (39)$$

Within the left softening length, i.e. $0 \leq x < L_{s1}$, and based on Eqs. (28) and (30), the slip δ_{sl1} and normal stress $\sigma_{g,sl1}$ of the GFRP component can be expressed as:

$$\delta_{sl1}(x) = C_2 \sin(\lambda_2 x) + D_2 \sinh(\lambda_2 x) + \delta_f \quad (40)$$

$$\sigma_{g,sl1}(x) = \eta \left[\frac{P_{u,s2}}{E_s A_s} - \lambda_2 C_2 \cos(\lambda_2 x) + \lambda_2 D_2 \sin(\lambda_2 x) \right] \quad (41)$$

where the subscript 'sl1' refers to the left softening length.

Within the right softening length, i.e. $L_{s1} + L_e < x \leq L$ (Fig. 8), and also based on Eqs. (28) and (30), slip δ_{sl2} and normal stress $\sigma_{g,sl2}$ of the GFRP component can be expressed as:

$$\delta_{sl2}(x) = C_3 \sin[\lambda_2(x - L_{s1} - L_e)] + D_3 \sinh[\lambda_2(x - L_{s1} - L_e)] + \delta_f \quad (42)$$

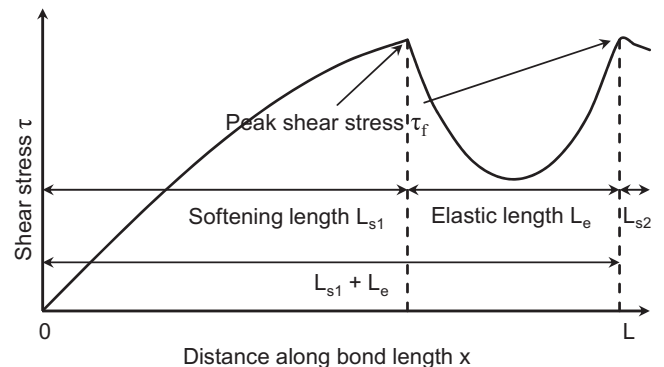


Fig. 8. Typical shear stress distribution when $P = P_{u,s2}$ (softening of both ends).

$$\sigma_{g,sl2}(x) = \eta \left[\frac{P_{u,s2}}{E_s A_s} - \lambda_2 C_3 \cos[\lambda_2(x - L_{s1} - L_e)] + \lambda_2 D_3 \sin[\lambda_2(x - L_{s1} - L_e)] \right] \quad (43)$$

where the subscript 'sl2' refers to the right softening length.

The values of A_3 , B_3 , C_2 , D_2 , C_3 , D_3 , $P_{u,s2}$, L_{s1} , L_e can be determined by applying the following nine boundary conditions:

$$\delta_{sl1}(x=0) = \delta_f \quad (44)$$

$$\delta_{sl1}(x=L_{s1}) = \delta_1 \quad (45)$$

$$\delta_{el}(x=L_{s1}) = \delta_1 \quad (46)$$

$$\delta_{el}(x=L_{s1} + L_e) = \delta_1 \quad (47)$$

$$\delta_{sl2}(x=L_{s1} + L_e) = \delta_1 \quad (48)$$

$$\sigma_{g,sl1}(x=0) = \frac{P_{u,s2}}{A_g} \quad (49)$$

$$\sigma_{g,sl2}(x=L) = 0 \quad (50)$$

$$\sigma_{g,sl1}(x=L_{s1}) = \sigma_{g,el}(x=L_{s1}) \quad (51)$$

$$\sigma_{g,el}(x=L_{s1} + L_e) = \sigma_{g,sl2}(x=L_{s1} + L_e) \quad (52)$$

When $P = P_{u,s2}$, the resulting shear stress at a given location x along the bond length $\tau(x)$ can be calculated from Eq. (53):

$$\tau(x) = \begin{cases} \frac{\tau_f}{\delta_f - \delta_1} [\delta_f - \delta_{sl1}(x)], & 0 \leq x \leq L_{s1} \\ \frac{\tau_f}{\delta_1} \delta_{el}(x), & L_{s1} < x \leq L_{s1} + L_e \\ \frac{\tau_f}{\delta_f - \delta_1} [\delta_f - \delta_{sl2}(x)], & L_{s1} + L_e < x \leq L \end{cases} \quad (53)$$

If the applied load P continuously increases from P_e to the ultimate load $P_{u,s2}$, one end of the bond length (i.e. the GFRP end) starts to soften first, followed by the softening of both ends and then pull-out failure occurs when the debonding slip δ_f is attained at the GFRP end. Thus the form of shear stress distribution changes accordingly, depending on the applied load level. When $P_e < P < P_{u,s2}$, shear stress distribution $\tau(x)$ thus may involve the softening of one or both ends, depending on the load level. It is also necessary to check that at this ultimate state (when $P = P_{u,s2}$), the slip at the steel end is within the softening region (i.e. $\delta_1 < \delta_{sl2}(x=L) < \delta_f$), and the softening length at the steel end is positive (i.e. $L_{s2} > 0$).

3.6. Joint capacity $P_{u,sf}$ at ultimate state for softening of full bond length

This ultimate state corresponds to the scenario in which the full bond length is loaded into the softening stage of the bilinear bond-slip curve (i.e. $L = L_s$) and the peak shear stress τ_f is achieved within the bond length at a location $x = L_p$, as illustrated by Fig. 9.

As $L = L_s$ and based on Eqs. (28) and (30), the slip δ_{sl} and normal stress of the GFRP component $\sigma_{g,sl}$ can be expressed as:

$$\delta_{sl}(x) = C_2 \sin(\lambda_2 x) + D_2 \sinh(\lambda_2 x) + \delta_f \quad (54)$$

$$\sigma_{g,sl}(x) = \eta \left[\frac{P_{u,sf}}{E_s A_s} - \lambda_2 C_2 \cos(\lambda_2 x) + \lambda_2 D_2 \sin(\lambda_2 x) \right] \quad (55)$$

When this ultimate state is attained, i.e. $P = P_{u,sf}$ (the subscript 'sf' denotes softening of the full bond length), the peak shear stress τ_f appears at the location $x = L_p$, and the values of C_2 , D_2 , $P_{u,sf}$, L_p can be determined by applying the following four boundary conditions:

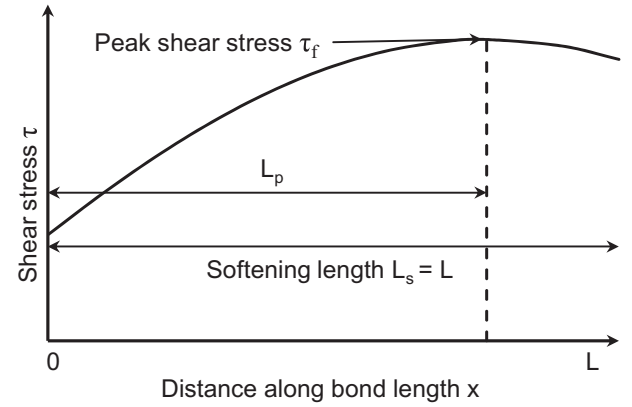


Fig. 9. Typical shear stress distribution when $P = P_{u,sf}$ (softening of full bond length).

$$\delta_{sl}(x=L_p) = \delta_1 \quad (56)$$

$$\frac{d\delta_{sl}}{dx}(x=L_p) = 0 \quad (57)$$

$$\sigma_{g,sl}(x=0) = \frac{P_{u,sf}}{A_g} \quad (58)$$

$$\sigma_{g,sl}(x=L) = 0 \quad (59)$$

The corresponding shear stress distribution $\tau(x)$ can be formed by Eq. (60) for this ultimate state.

$$\tau(x) = \frac{\tau_f}{\delta_f - \delta_1} [\delta_f - \delta_{sl}(x)], \quad 0 \leq x \leq L \quad (60)$$

When the applied load increases from P_e to $P_{u,sf}$, softening of one end is initiated first (i.e. the GFRP end), followed by softening of the other end, and finally the two softening regions merge into one (i.e. $L_s = L$) and pull-out failure occurs. The forms of shear stress distribution may change accordingly, depending on the applied load level. When $P_e < P < P_{u,s2}$, shear stress distribution $\tau(x)$ thus may involve softening of one or two ends, depending on the load level. Again, it is necessary to validate this ultimate state (when $P = P_{u,sf}$) by checking that the slip at the GFRP end is within the softening stage (i.e. $\delta_1 < \delta_{sl}(x=0) < \delta_f$) and the same condition at the steel end (i.e. $\delta_1 < \delta_{sl}(x=L) < \delta_f$).

It should be noted that failure may also occur in the steel or GFRP component if the joint capacity is greater than the axial capacity of the adherend components. In this case, the joint capacity P_s is determined by the steel yielding strength as $A_s f_{sy}$ or by the GFRP tensile strength as $A_g f_{gu}$, where f_{sy} and f_{gu} are the yield strength and ultimate strength of the steel and GFRP component respectively.

4. FE analysis

4.1. Geometry and materials

FE analysis was conducted using the ANSYS package to describe the mechanical response of bonded sleeve joints under axial tension. Fig. 10a presents an example of the geometry of a bonded sleeve joint connecting steel and GFRP tubes. Focusing on verifying the theoretical results and estimating the experimental pull-out failure load, the FE models were constructed only concerning the bonded regions of the specimens. The material properties of the GFRP, steel and adhesive are provided in Table 1. The GFRP was defined as a linearly elastic and transversely isotropic material with its longitudinal direction in alignment with the x -axis

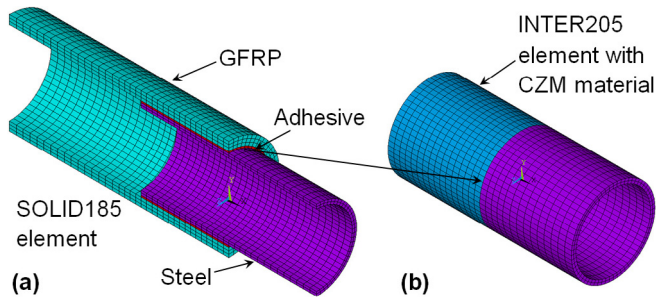


Fig. 10. FE modelling: (a) overall geometry; (b) interface elements.

(Fig. 10a). An isotropic bilinear work hardening material model was employed for the steel component, with Von Mises's yield criterion and flow rule after yielding. The post-yield hardening modulus of the steel was taken 2% of its Young's modulus ($2\% E_s$), an upper limit of practical steel material as suggested in [50]. The material definition for the adhesive was isotropic and linearly elastic.

4.2. Model establishment

All elements of the GFRP, steel and adhesive components were meshed in ANSYS with SOLID185, a 3-D 8-node element. Three or seven layers of elements were used across the thickness of each GFRP tube or rod, while two layers were used for the steel and one for the adhesive. Success in simulating bonded zone behaviour hinges on correct implementation of the cohesive zone modelling (CZM) technique in ANSYS. In general, the pull-out failure observed from experiments took place in the adhesive layer (near the inner adherend) or at the adhesive-inner adherend interface. This is because of the slightly smaller bonded area associated to the inner adherend, thus larger shear stress on the inner surface of the adhesive layer. Accordingly, INTER205, a planar 3-D 8-node cohesive element, was applied between the adhesive and the inner adherend (Fig. 10b). This 8-node element has four pairs of overlapping nodes; each pair is attached to adjacent elements of steel and adhesive or GFRP and adhesive. The overlapping nodes were separated upon loading through a 'Mode II' separation, parallel to the bonded interface, as observed from the experiments (Fig. 3a). The shear traction–separation relationship was defined with the CZM material property option in ANSYS, and was established in accordance to the bilinear bond-slip relationship presented in Fig. 5. Mesh studies were performed for specimens in G2 and G5 with respect to the number of elements along the bond length, ensuring that further refinement resulted in less than 1% change in the ultimate joint capacities. As a result, elements sized at approximately 2 mm in the bond length direction were adopted.

4.3. Boundary condition and loading

In application of the axial loading, the GFRP end was restrained in all directions before the steel end was displaced in a tensile manner until the ultimate load was attained. Effects of material nonlinearity were accounted for. The displacement was applied in two load steps and solved with the sparse direct equation solver. The first load step was a ramped-load where the displacement was increased uniformly. As the ultimate load was approached, a second load step was introduced for better convergence, in which the automatic time stepping option was activated. This enabled the program to determine the size of displacement increment based on the structural response, and upon convergence failure

after a certain number of iterations, to restart with a halved increment size.

5. Results and discussion

5.1. Comparison of ultimate joint capacity

Summarised in Table 2 are the experimental results of the ultimate joint capacities ($P_{u,E}$), along with theoretical estimates $P_{u,TH}$ (either $P_{u,s1}$, $P_{u,s2}$ or $P_{u,sf}$) and numerical estimates ($P_{u,FE}$) for the specimens observed with the pull-out failure mode. Among these 14 specimens, the average ratio between experimental and theoretical results of joint capacity ($P_{u,E}/P_{u,TH}$) was 0.935 and that between experimental and FE results ($P_{u,E}/P_{u,FE}$) was 0.981, with standard deviations of 0.114 and 0.095 respectively. These indicated good prediction and slight overestimation by the theoretical and FE modelling, which may be attributed to fabrication defects in the bonding zones of the specimens examined in the experiments.

According to the theoretical and FE modelling of all the experimental specimens, their ultimate states were achieved when the full bond length was loaded into the softening stage, i.e. $P = P_{u,sf}$, therefore the resulting shear stress distribution was formulated in Section 3.6. Because the same bond-slip relationship was used, it was anticipated that close values of ultimate joint capacity (i.e. $P_{u,TH}$ vs. $P_{u,FE}$) would be obtained from the theoretical and FE modelling. However, the FE modelling produced slightly lower estimates than the theoretical ones (the average ratio $P_{u,FE}/P_{u,TH}$ was 0.952). This may be attributed to a smaller bonded circumference outside the inner adherend in the FE modelling compared to that defined at the adhesive centreline in the theoretical formulation, i.e. due to the assumption of a thin adhesive layer. Still, a discrepancy to notice is that, besides the yielding of steel, the FE modelling further considered shear deformation of adherends whereas the theoretical formulation did not. The effects of shear deformation of adherends may be taken into account by adopting the improved Volkersen method developed in [51]. Such effects were revealed by trial FE analysis to be insignificant and were thus neglected in the theoretical formulation. It should be noted that FE modelling was also conducted for the same specimens under compression loading. Identical joint capacity and adhesive shear stress distribution were produced as those under tension, which was also in accordance to the theoretical formulation.

5.2. Shear stress distribution

Verified against the experimental ultimate joint capacities, the theoretical and FE modelling are capable of providing insight into the shear stress distribution, which is difficult to measure from experiments. Fig. 11 shows examples of three forms of shear stress distribution corresponding to different states of joint capacity through theoretical and FE modelling. Using specimen G1-50 as an example, Figs. 11a or 10b present the stress distribution when the applied load P reached P_e or $P_{u,sf}$. In Fig. 11a, the full bond length was in the elastic stage (i.e. $\delta \leq \delta_1$ and $L = L_e$) with the peak shear stress τ_f attained at the GFRP end. The FE modelling gave higher estimates of slip δ (or shear stress τ) in the middle portion, resulting in 12.4% overestimation of P_e . For the same specimen, in Fig. 11b, the full bond length was in the softening stage (i.e. $\delta_1 \leq \delta < \delta_f$ and $L = L_s$) corresponding to the joint capacity $P_{u,sf}$ of 53.9 kN by theoretical formulation or 51.6 kN by FE modelling. The peak shear stress τ_f appeared closer to the steel end, indicating that the GFRP end was subjected to higher level of slip. The shear stress distributions provided by theoretical and FE modelling were practically identical.

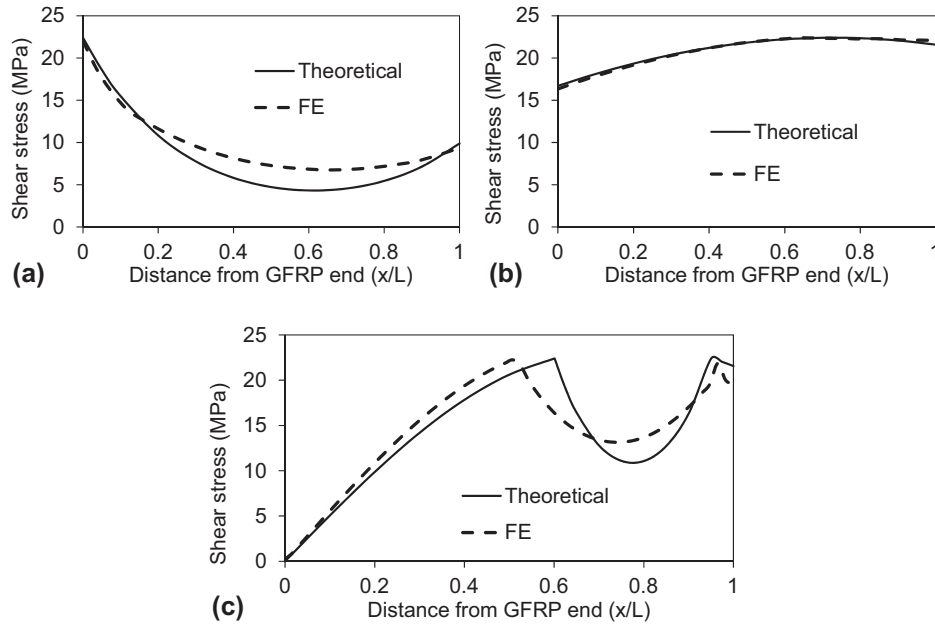


Fig. 11. Shear stress distribution along bond length: (a) specimen G1-50 when $P = P_e$ (20.9 kN or 23.5 for theoretical or FE modelling); (b) specimen G1-50 when $P = P_{u,sf}$ (53.9 kN or 51.6 kN for theoretical or FE modelling); (c) theoretical and FE example G2-140 when $P = P_{u,s2}$ (167.8 kN or 160.4 kN for theoretical or FE modelling).

The section configuration of specimens G2, with a longer bond length of 140 mm, can be used for theoretical and numerical investigation. Fig. 11c presents the shear stress distribution when $P = P_{u,s2}$, i.e. softening occurred at both ends and the debonding slip δ_f was attained at the GFRP end. In Fig. 11c, the two peaks, representing the peak shear stress τ_f , divide the full bond length into three portions: L_{s1} , L_e and L_{s2} from left to right. This was in accordance with the form of shear stress distribution presented in Fig. 8. Compared to the theoretical distribution, the FE result exhibited shorter L_{s1} (84.6% of the theoretical result) and longer L_e (130.6% of the theoretical result). In general, however, a satisfactory agreement of joint capacity $P_{u,s2}$ can be found from Fig. 11c. It should be noted that experimentally such a specimen would fail in the steel component because of the joint capacity being greater than the 118.4 kN of the steel adherend.

Fig. 12 shows, through FE analysis, the adhesive shear stress distribution at different load levels. For both the specimen G1-50 and the numerical example of G2-140, when the applied load (85% P_e in Fig. 12a and b) was less than P_e , the full bond length remained in the elastic stage and the maximum shear stress appeared at the GFRP end due to its lower stiffness ($E_g A_g$). As the axial load (85% $P_{u,sf}$ in Fig. 12a and 85% $P_{u,s2}$ in Fig. 12b) increased beyond the elastic limit while still below the ultimate state (i.e.

$P_e < P < P_{u,sf}$ or $P_{u,s2}$), softening was introduced at the GFRP end, resulting in the peak shear stress (τ_f) appearing and shifting towards the steel end while the rest of bond length remained in the elastic stage. Approaching the ultimate state, specimen G1-50 (see Fig. 12a) had softening at both ends, and these two regions merged into one when the load increased to 100% $P_{u,sf}$, resulting in softening of the entire bond length. The peak shear stress (τ_f) appeared at the confluence point of the two softening regions, i.e. at the location of L_p in Fig. 9. In contrast, for the numerical example G2-140 at 100% $P_{u,s2}$ (see Fig. 12b), where the ultimate state corresponds to softening of both ends, the softening length at the GFRP end extended towards the steel end such that the slip $\delta(x/L = 0)$ reached δ_f . Meanwhile, softening was also introduced at the steel end (i.e. $\delta_1 < \delta(x/L = 1) < \delta_f$). The peak shear stress (τ_f), appearing at two locations corresponding to those of L_{s1} and $L_{s1} + L_{se}$ (also see Fig. 8), defines the boundaries of the bond length remaining in the elastic stage.

5.3. Effect of bond length on joint capacity

Variation of bond length (L), resulting in different forms of shear stress distribution as illustrated in the theoretical formulation, is believed to have a significant effect on the joint capacity. Fig. 13

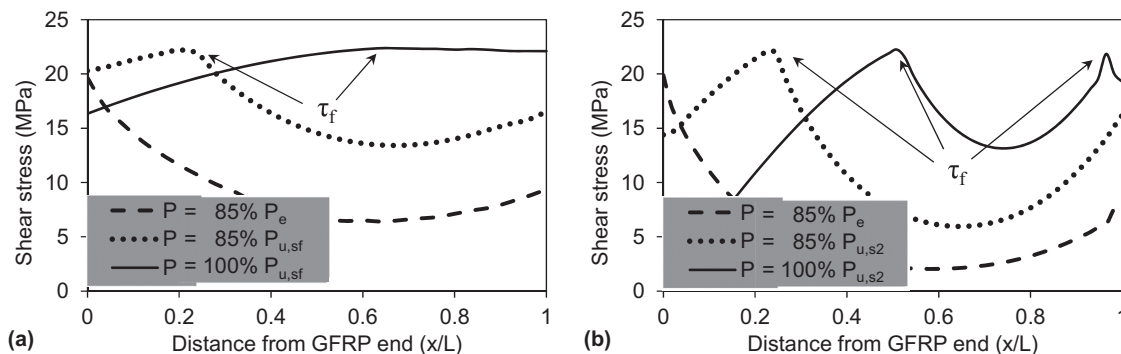


Fig. 12. Shear stress distribution along bond length from FE modelling at different load level: (a) specimen G1-50; (b) FE example G2-140.

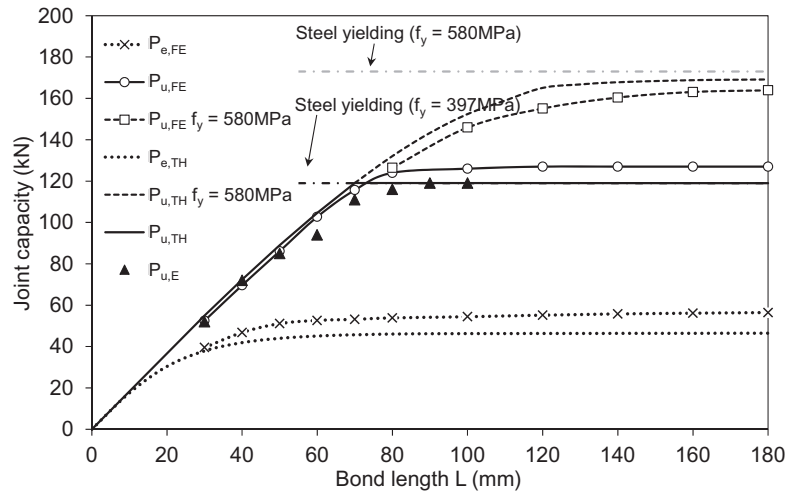


Fig. 13. Effect of bond length on joint capacity (specimens based on cross-section configuration in G2).

presents the results of a parametric study with respect to bond length (L), using section configuration of specimens G2. Both the theoretical and the FE results in Fig. 13 indicated that the joint capacity at the elastic limit P_e ceased to improve when the bond length reached a certain level, demonstrating the existence of an effective bond length within the elastic stage, which in this case was around 40 mm. For bond lengths longer than the effective value, the theoretical and FE modelling presented joint capacity P_e around 46 kN and 55 kN respectively.

Clearly, the applied load may be increased beyond the elastic stage. Experimental, theoretical and FE results of the relationship between ultimate joint capacity and bond length are also presented in Fig. 13. Represented by the black triangles, the experimental results increased almost linearly until a bond length of around 70 mm, after which little improvement in joint capacity was observed, due to yielding of the steel tube connector as observed from experiments. The theoretical and FE results, showing similar patterns, produced close agreement to experimental data. It is worth clarifying that steel yielding was considered in both theoretical and FE calculations, resulting in the joint capacity at 119 kN and 126 kN formed as a horizontal line as the representation of the capacity of the steel tube connector.

Furthermore, in order to investigate the effect of bond length on ultimate joint capacity that is dominated not by adherend capacity (e.g. steel yielding) but by adhesive bonding, theoretical and FE modelling were conducted on a series of specimens with the same cross-section configuration as those in G2 but with the different steel yield strength (f_{sy}) of 580 MPa. Shown in Fig. 13, the theoretical and FE ultimate joint capacities of such specimens still reached a plateau that was not defined by the capacity of the adherends (steel yielding in this case), corresponding to an effective bond length of around 125 mm at the ultimate state. At and beyond this effective value, the ultimate joint capacity was calculated as 169 kN from theoretical modelling and 163 kN from FE modelling.

It is also worthwhile to examine the change in the form of shear stress distribution at the ultimate state of adhesive bonding (rather than adherend) when the bond length approached the effective value. For the section configuration G2 with steel yield strength (f_{sy}) of 580 MPa, Fig. 14a shows that, at the bond length of 100 mm (slightly below the effective value of 125 mm), the type of shear stress distribution at the ultimate state (i.e. $P = P_{u,sf}$) was characterised by softening of the full bond length. In contrast, with a bond length of 120 mm, which was close to the effective value, Fig. 14b shows the type of distribution when softening occurred

at both ends, with the debonding slip δ_f attained at the GFRP end, corresponding to the ultimate state illustrated in Fig. 8, i.e. $P = P_{u,s2}$. This outcome occurred because, as the bond length became sufficiently long, the debonding slip δ_f was attained at one end before the two softening ends merged. It should also be noted that as the bond length passed the effective value, other than the change of ultimate state from $P_{u,sf}$ to $P_{u,s2}$ as illustrated above, a change from $P_{u,sf}$ to $P_{u,s1}$ could also occur depending on the section geometries and bond-slip parameters. Similarly, this change was due to the redistribution of shear stress. With a sufficiently long bond length, the debonding slip δ_f might be attained at one end before the other was loaded into the softening stage.

5.4. Effect of stiffness ratio on joint capacities

The stiffness ratio between adherends (i.e. $E_s A_s / E_g A_g$) is another important parameter to be considered in the design of such bonded sleeve connections. In previous elastic analysis of single or double lap joints, the inequality between $E_s A_s$ and $E_g A_g$, known as the adherend stiffness imbalance, could cause incapacity of a joint to develop full strength at the elastic stage. This is because the bonded zone at the end with the less stiff adherend could be loaded to its stress limit prior to the other end [32,52,53]. Using the developed theoretical formulation, the effect of this stiffness imbalance on both the elastic and the ultimate state joint capacity of a bonded sleeve connection is illustrated in Fig. 15, based on the cross-section configurations and bond length of specimen G5-80. The variation of stiffness ratios was achieved by changing the outer diameter of the GFRP tube or the inner diameter of the steel tube, while maintaining the section geometry of the adhesive layer. This resulted in stiffness ratios $E_s A_s / E_g A_g$ from 0.2 to 4 as shown in Fig. 15.

Fig. 15 shows that, consistent with the cases of single or double lap joints, the greatest joint capacity at the elastic limit (P_e) of a bonded sleeve connection was achieved when the of the adherends had equal stiffness i.e. $E_s A_s / E_g A_g = 1$. At the ultimate state (in this case $P_{u,sf}$), the greatest joint capacity was achieved at a stiffness ratio of around 0.8, as shown in Fig. 15. The variation of joint capacity at the elastic limit (P_e) with the stiffness ratio $E_s A_s / E_g A_g$ was much more significant than that at the ultimate state ($P_{u,sf}$). This finding is attributed to the steeper slope of the bilinear bond-slip relationship at the elastic stage than at the softening stage (see Fig. 5). Similar results were also observed from such

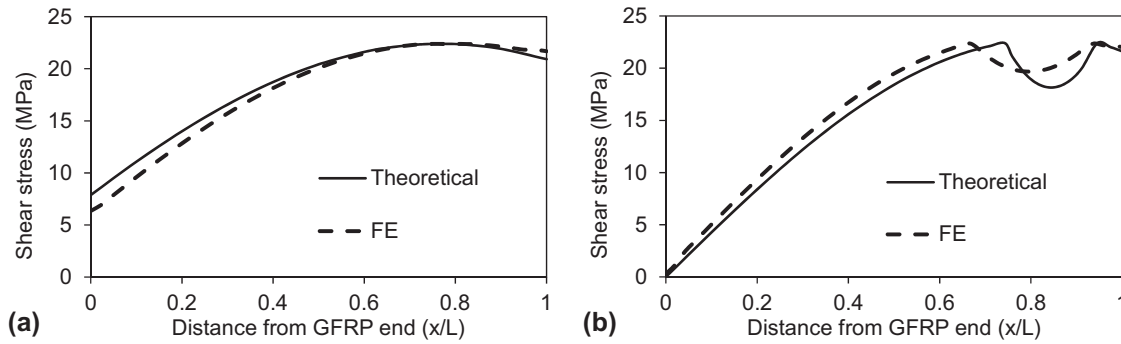


Fig. 14. Change of shear stress distribution form as bond length approached effective value: (a) G2-100 with elevated adherend strength ($P_{u,sf} = 152.4$ kN or 145.9 kN for theoretical or FE modelling); (b) G2-120 with elevated adherend strength ($P_{u,s2} = 165.1$ kN or 155.8 kN for theoretical or FE modelling).

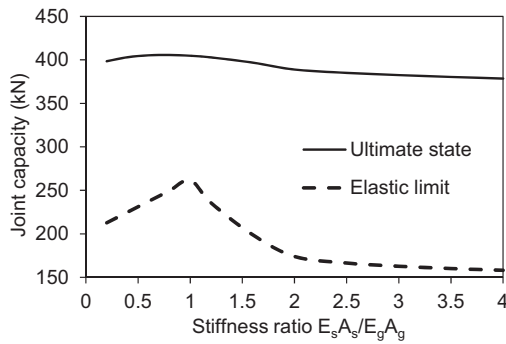


Fig. 15. Effect of stiffness ratio ($E_s A_s / E_g A_g$) on joint capacity at elastic limit (P_e) and at ultimate state ($P_{u,sf}$) based on specimen G5-80.

investigations on specimens with other section configurations and bond lengths.

Fig. 16 shows the shear stress distribution calculated by the theoretical formulation for the configuration of specimen G5-80 with three stiffness ratios. For the elastic limit, i.e. $P = P_e$, Fig. 16a indicates that the shear stress distribution was symmetrical when $E_s A_s / E_g A_g = 1$, and the peak shear stress τ_f was attained simultaneously at both ends. Otherwise, for the unbalanced stiffness ratios (i.e. $E_s A_s / E_g A_g = 0.4$ or 2.5), the peak shear stress τ_f only appeared at the end of the less stiff adherend. Fig. 16b presents the shear stress distribution at the ultimate state, i.e. $P = P_{u,sf}$. Likewise, the balanced adherend stiffness (i.e. $E_s A_s / E_g A_g = 1$) produced a symmetrical shear stress distribution which had the peak shear stress τ_f appear at the middle of the bond length. The unbalanced adherend stiffness resulted in the peak shear stress τ_f being located closer to

the end of the stiffer adherend, indicating a higher level of slip δ at the other end.

6. Conclusions

This paper develops a theoretic formulation to describe the adhesive shear stress distribution and to predict the joint capacity of bonded sleeve connections. A bilinear bond-slip relationship was implemented in the governing equations to consider the elastic, softening and debonding behaviour of the adhesive bonding. The results of ultimate joint capacity calculated by the theoretic formulation were validated by results from FE modelling and from experimental specimens subjected to axial tension where various cross-sections and bond lengths were covered. Utilising the validated theoretic and FE modelling, the effects of bond length and stiffness ratio on the adhesive shear stress distribution and joint capacity were discussed and clarified for such bonded sleeve connections. The work presented in this paper allows the following conclusions to be drawn:

1. Employing the bilinear bond-slip relationship, when the bonded sleeve connection is loaded to elastic limit, the full bond length is within the elastic stage and the peak shear stress (τ_f) appears at the end of the less stiff adherend. The joint capacity at the ultimate state shows three different scenarios, each corresponding to shear stress distribution that features softening of one end or both ends or along the full length of the bonding region. The theoretic formulation, developed based on linear elastic adherends, gives satisfactory prediction of the pull-out joint capacities for the experimental specimens with different cross-sections and bond lengths; the average test/prediction ratio was obtained as 0.935.

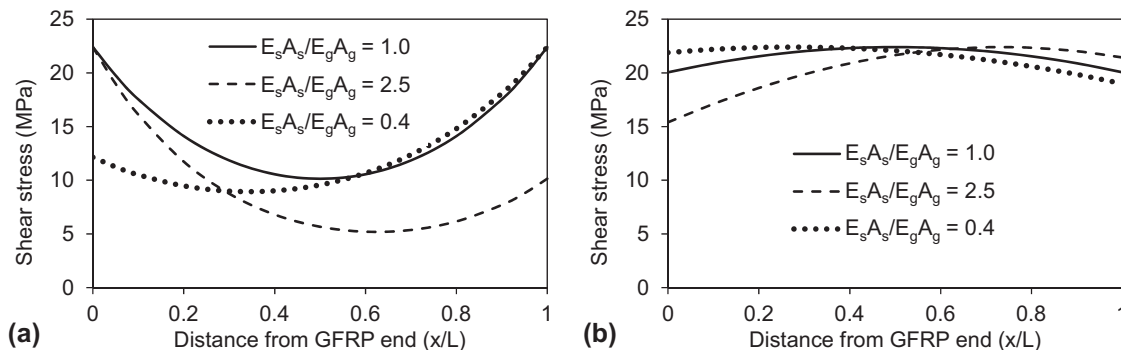


Fig. 16. Effect of stiffness ratio ($E_s A_s / E_g A_g$) on shear stress distribution from theoretical modelling based on specimen G5-80: (a) when $P = P_e$; (b) when $P = P_{u,sf}$.

2. FE modelling can simulate adhesive bonding using the cohesive interface elements associated with Mode II separation and the bilinear bond-slip relationship. The FE modelling produced slightly lower joint capacities compared to the theoretical modelling, which could be explained by the more conservative representation of the actual bond area in the FE modelling and the consideration of material nonlinearity in the adherend. The FE modelling yielded accurate prediction of the experimental joint capacities for the pull-out failure mode, with an average test/prediction ratio of 0.981.
3. For cases with no adherend failure, effective bond lengths do exist for the joint capacities at both the elastic limit and the ultimate state. Beyond the effective lengths, no further increase in joint capacity was observed. Such effective bond lengths can be well identified by the theoretic formulation and further well validated by the FE modelling results. Attainment of effective bond length may further cause transformation of the shear stress distribution at the ultimate state. For example, the ultimate state of $P_{u,sf}$ may change to $P_{u,s2}$ if the bond length increases from 100 mm to 120 mm for the G2 cross-section. Such transformation of shear stress distribution may also occur from $P_{u,sf}$ to $P_{u,s1}$ depending on the cross-section configuration or bond-slip parameters. Finally, taking into account the capacity of adherends, the relationship between bond length and ultimate joint capacity can be developed via theoretical and FE modelling for a specific bonded sleeve connection.
4. The maximum joint capacity at the elastic limit (P_e) occurs when the stiffnesses of adherends are balanced (i.e. $E_s A_s / E_g A_g = 1$). This finding is consistent with those from single or double lap joints. Whereas the joint capacity at the ultimate state ($P_{u,s}$) is optimal at the stiffness ratio ($E_s A_s / E_g A_g$) of around 0.8, the effect of this stiffness ratio on the ultimate joint capacity is much less obvious in comparison to the effect on the elastic joint capacity. For both the elastic limit and ultimate state, a balanced adherend stiffness (i.e. $E_s A_s / E_g A_g = 1$) generates symmetrical shear stress distribution, while a difference in adherend stiffness (i.e. $E_s A_s / E_g A_g \neq 1$) leads to more slip (δ) at the end of the less stiff adherend.

Acknowledgments

The authors gratefully acknowledge the support from the ARC Training Centre for Advanced Manufacturing of Prefabricated Housing (IC150100023) and the National Natural Science Foundation of China (No. 51522807).

References

- [1] Bakis C, Bank LC, Brown V, Cosenza E, Davalos J, Lesko J, et al. Fiber-reinforced polymer composites for construction-state-of-the-art review. *J Compos Constr* 2002;6(2):73–87.
- [2] Hollaway L. A review of the present and future utilisation of FRP composites in the civil infrastructure with reference to their important in-service properties. *Constr Build Mater* 2010;24(12):2419–45.
- [3] Nagaraj V, GangaRao HV. Static behavior of pultruded GFRP beams. *J Compos Constr* 1997;1(3):120–9.
- [4] Di Tommaso A, Russo S. Shape influence in buckling of GFRP pultruded columns. *Mech Compos Mater* 2003;39(4):329–40.
- [5] Keller T, Schollmayer M. Plate bending behavior of a pultruded GFRP bridge deck system. *Compos Struct* 2004;64(3):285–95.
- [6] Bank LC. *Composites for construction: structural design with FRP materials*. New York: John Wiley & Sons; 2006.
- [7] Meyer R. *Handbook of pultrusion technology*. Springer Science & Business Media; 2012.
- [8] Bank LC, Gentry TR, Nuss KH, Hurd SH, Lamanna AJ, Duich SJ, et al. Construction of a pultruded composite structure: case study. *J Compos Constr* 2000;4(3):112–9.
- [9] Keller T. *Use of fibre reinforced polymers in bridge construction*. Zurich: International Association for Bridge and Structural Engineering (IABSE); 2003.
- [10] Turner MK, Harries KA, Petrou MF, Rizos D. In situ structural evaluation of a GFRP bridge deck system. *Compos Struct* 2004;65(2):157–65.
- [11] Zou X, Feng P, Wang J. Perforated FRP ribs for shear connecting of FRP-concrete hybrid beams/decks. *Compos Struct* 2016;152:267–76.
- [12] Benmokrane B, El-Salakawy E, El-Gamal S, Goulet S. Construction and testing of an innovative concrete bridge deck totally reinforced with glass FRP bars: Val-Alain Bridge on Highway 20 East. *J Bridge Eng* 2007;12(5):632–45.
- [13] Keller T, Haas C, Vallée T. Structural concept, design, and experimental verification of a glass fiber-reinforced polymer sandwich roof structure. *J Compos Constr* 2008;12(4):454–68.
- [14] Hagio H, Utsumi Y, Kimura K, Takahashi K, Itohiya G, Tazawa H. Development of space truss structure using glass fiber reinforced plastics. *Proceedings: Advanced Materials for Construction of Bridges, Buildings, and Other Structures III*, Davos, Switzerland, 7–12 September 2003. ECI Digital Archives.
- [15] Awad ZK, Aravinthan T, Zhuge Y. Experimental and numerical analysis of an innovative GFRP sandwich floor panel under point load. *Eng Struct* 2012;41:126–35.
- [16] Satasivam S, Bai Y, Zhao X-L. Adhesively bonded modular GFRP web-flange sandwich for building floor construction. *Compos Struct* 2014;111:381–92.
- [17] Satasivam S, Bai Y. Mechanical performance of bolted modular GFRP composite sandwich structures using standard and blind bolts. *Compos Struct* 2014;117:59–70.
- [18] Feng P, Cheng S, Bai Y, Ye L. Mechanical behavior of concrete-filled square steel tube with FRP-confined concrete core subjected to axial compression. *Compos Struct* 2015;123:312–24.
- [19] Feng P, Zhang Y, Bai Y, Ye L. Combination of bamboo filling and FRP wrapping to strengthen steel members in compression. *J Compos Constr* 2013;17(3):347–56.
- [20] Feng P, Zhang Y, Bai Y, Ye L. Strengthening of steel members in compression by mortar-filled FRP tubes. *Thin-Walled Struct* 2013;64:1–12.
- [21] Smith S, Parsons I, Hjelmstad K. An experimental study of the behavior of connections for pultruded GFRP I-beams and rectangular tubes. *Compos Struct* 1998;42(3):281–90.
- [22] Smith S, Parsons I, Hjelmstad K. Experimental comparisons of connections for GFRP pultruded frames. *J Compos Constr* 1999;3(1):20–6.
- [23] Singamsethi S, LaFave J, Hjelmstad K. Fabrication and testing of cuff connections for GFRP box sections. *J Compos Constr* 2005;9(6):536–44.
- [24] Yang X, Bai Y, Luo FJ, Zhao X-L, He X. Fiber-reinforced polymer composite members with adhesive bonded sleeve joints for space frame structures. *J Mater Civ Eng* 2016;04016208.
- [25] Yang X, Bai Y, Ding F. Structural performance of a large-scale space frame assembled using pultruded GFRP composites. *Compos Struct* 2015;133:986–96.
- [26] Luo FJ, Bai Y, Yang X, Lu Y. Bolted sleeve joints for connecting pultruded FRP tubular components. *J Compos Constr* 2016;20(1):04015024.
- [27] Luo FJ, Yang X, Bai Y. Member capacity of pultruded GFRP tubular profile with bolted sleeve joints for assembly of latticed structures. *J Compos Constr* 2016;20(3):04015080.
- [28] Wu C, Zhang Z, Bai Y. Connections of tubular GFRP wall studs to steel beams for building construction. *Compos B Eng* 2016;95:64–75.
- [29] Volkersen O. Die Nietkraftverteilung in zugbeanspruchten Nietverbindungen mit konstanten Laschenquerschnitten. *Luftfahrtforschung* 1938;15(1/2):41–7.
- [30] Goland M, Reissner E. The stresses in cemented joints. *J Appl Mech* 1944;11(1):A17–27.
- [31] Hart-Smith LJ. *Adhesive-bonded single-lap joints*. Hampton: National Aeronautics and Space Administration; 1973.
- [32] Hart-Smith LJ. *Adhesive-bonded double-lap joints*. Hampton: National Aeronautics and Space Administration; 1973.
- [33] Ranisch E-H. Zur Tragfähigkeit von Verklebungen zwischen Baustahl und Beton: geklebte Bewehrung. *Inst. für Baustoffe, Massivbau und Brandschutz der Techn. Univ.*; 1982.
- [34] Brosens K, Van Gemert D. Plate end shear design for external CFRP laminates. In: *Fracture Mechanics of Concrete Structures*, vol. 3. AEDIFICATIO Publishers, 1998. p. 1793–804.
- [35] Yuan H, Teng J, Seracino R, Wu Z, Yao J. Full-range behavior of FRP-to-concrete bonded joints. *Eng Struct* 2004;26(5):553–65.
- [36] Wu Z, Yuan H, Niu H. Stress transfer and fracture propagation in different kinds of adhesive joints. *J Eng Mech* 2002;128(5):562–73.
- [37] Holzenkämpfer P. *Ingenieurmodelle des Verbunds geklebter Bewehrung für Betonbauteile* 1997.
- [38] Xia S, Teng J. Behaviour of FRP-to-steel bonded joints. *Proceedings of the international symposium on bond behaviour of FRP in structures: International Institute for FRP in Construction*; 2005. p. 419–26.
- [39] Campilho R, De Moura M, Domingues J. Modelling single and double-lap repairs on composite materials. *Compos Sci Technol* 2005;65(13):1948–58.
- [40] Campilho R, Banea MD, Pinto A, da Silva LF, De Jesus A. Strength prediction of single- and double-lap joints by standard and extended finite element modelling. *Int J Adhes Adhes* 2011;31(5):363–72.
- [41] Nakaba K, Kanakubo T, Furuta T, Yoshizawa H. Bond behavior between fiber-reinforced polymer laminates and concrete. *Struct J* 2001;98(3):359–67.
- [42] Wu Z, Yin J. Fracturing behaviors of FRP-strengthened concrete structures. *Eng Fract Mech* 2003;70(10):1339–55.
- [43] Fawzia S, Zhao X-L, Al-Mahaidi R. Bond-slip models for double strap joints strengthened by FRP. *Compos Struct* 2010;92(9):2137–45.
- [44] Yu T, Fernando D, Teng J, Zhao X. Experimental study on CFRP-to-steel bonded interfaces. *Compos B Eng* 2012;43(5):2279–89.

- [45] Täljsten B. Strengthening of concrete prisms using the plate-bonding technique. *Int J Fract* 1996;82(3):253–66.
- [46] Yuan H, Wu ZS, Yoshizawa H. Theoretical solutions on interfacial stress transfer of externally bonded steel/composite laminates. *J Struct Mech Earthquake Eng* 2001;675:27–39.
- [47] Campilho R, De Moura M, Domingues J. Using a cohesive damage model to predict the tensile behaviour of CFRP single-strap repairs. *Int J Solids Struct* 2008;45(5):1497–512.
- [48] Alfano G. On the influence of the shape of the interface law on the application of cohesive-zone models. *Compos Sci Technol* 2006;66(6):723–30.
- [49] Bai Y, Zhang C. Capacity of nonlinear large deformation for trusses assembled by brittle FRP composites. *Compos Struct* 2012;94(11):3347–53.
- [50] Kadin Y, Kligerman Y, Etsion I. Multiple loading–unloading of an elastic–plastic spherical contact. *Int J Solids Struct* 2006;43(22):7119–27.
- [51] Tsai M, Oplinger D, Morton J. Improved theoretical solutions for adhesive lap joints. *Int J Solids Struct* 1998;35(12):1163–85.
- [52] DoD (USA). Structural behaviour of joints, in: *Military Handbook – MIL-HDBK-17-3F: Composite Materials Handbook, Volume 3 – Polymer Matrix Composites Materials Usage, Design, and Analysis*, US Dept of Defense, Washington DC, 2002.
- [53] Al-Shawaf A. Understanding and predicting interfacial stresses in advanced fibre-reinforced polymer (FRP) composites for structural applications. *Advanced Fibre-Reinforced Polymer (FRP) Composites for Structural Applications* 2013:255.